Article

Investigation of Phase Segregation in *p*-Type Bi$_{0.5}$Sb$_{1.5}$Te$_3$ Thermoelectric Alloys by In Situ Melt Spinning to Determine Possible Carrier Filtering Effect

Dong Ho Kim [1,†], TaeWan Kim [2,†], Se Woong Lee [1], Hyun-Sik Kim [3], Weon Ho Shin [4] and Sang-il Kim [1,*]

1 Departament of Materials Science and Engineering, University of Seoul, Seoul 02504, Korea; hoo829@uos.ac.kr (D.H.K.); lswprawn245@uos.ac.kr (S.W.L.)
2 Departament of Electrical Engineering and Smart Grid Research Center, Jeonbuk National University, Jeonju 54896, Korea; twkim@jbnu.ac.kr
3 Departament of Materials Science and Engineering, Hongik University, Seoul 04066, Korea; hyunsik.kim@hongik.ac.kr
4 Departament of Electronic Materials Engineering, Kwangwoon University, Seoul 01897, Korea; weonho@kw.ac.kr
* Correspondence: sang1.kim@uos.ac.kr
† These authors contributed equally to this work.

Abstract: One means of enhancing the performance of thermoelectric materials is to generate secondary nanoprecipitates of metallic or semiconducting properties in a thermoelectric matrix, to form proper band bending and, in turn, to induce a low-energy carrier filtering effect. However, forming nanocomposites is challenging, and proper band bending relationships with secondary phases are largely unknown. Herein, we investigate the in situ phase segregation behavior during melt spinning with various metal elements, including Ti, V, Nb, Mo, W, Ni, Pd, and Cu, in *p*-type Bi$_{0.5}$Sb$_{1.5}$Te$_3$ (BST) thermoelectric alloys. The results showed that various metal chalcogenides were formed, which were related to the added metal elements as secondary phases. The electrical conductivity, Seebeck coefficient, and thermal conductivity of the BST composite with various secondary phases were measured and compared with those of pristine BST alloys. Possible band alignments with the secondary phases are introduced, which could be utilized for further investigation of a possible carrier filtering effect when forming nanocomposites.

Keywords: thermoelectric; phase segregation; melt spinning; carrier filtering effect

1. Introduction

Thermoelectric technology has attracted attention for its use in solid-state cooling and energy harvesting because it can convert heat directly into electricity. The energy conversion efficiency of thermoelectric materials is limited by the dimensionless figure of merit, $zT = [S^2 \cdot \sigma / (\kappa_{ele} + \kappa_{latt})] \times T$, where S is the Seebeck coefficient, σ is the electrical conductivity, κ_{ele} is the electronic thermal conductivity, κ_{latt} is the lattice thermal conductivity, and T is the absolute temperature [1–4]. Accordingly, a high zT value can be achieved by increasing $S^2 \cdot \sigma$ and reducing the thermal conductivities (κ_{ele} and κ_{latt}). However, these thermoelectric parameters are generally interdependent. Therefore, based on a comprehensive analysis of the fundamental mechanisms, thermoelectric materials should be manipulated to achieve optimal thermoelectric properties. In recent years, many approaches have been improved using zT values. Control of the carrier concentration, resonance doping, band engineering, and carrier filtering effects have been suggested for enhancing $S^2 \cdot \sigma$ [5–8]. However, other strategies exist for reducing thermal conductivity. These include inducing point defects, dislocation arrays, or nanostructures by increasing phonon scattering [9–12].

Of these approaches, carrier energy filtering can effectively improve zT by increasing S and $S^2 \cdot \sigma$. This type of filtering is achieved by energy barriers at heterointerfaces arising

from band bending between the thermoelectric matrix and secondary phases [13–15], which induce strong energy dependence on the carrier relaxation time. When proper phase segregation is introduced in thermoelectric materials, the carrier energy filtering effect can be achieved, thereby enhancing the thermoelectric performance through low-energy carrier scattering by potential heights formed at heterointerfaces [13,14]. In addition, phonon scattering can be strengthened by the segregated phases to reduce κ_{latt}.

Experimental evidence of *S* enhancement by the carrier filtering effect has been reported with various thermoelectric nanocomposites. Dou et al. reported an improvement in S of approximately 20%, as compared with that of the $Bi_{0.5}Sb_{1.5}Te_3$ matrix, which originated from the energy filtering of carriers [15]. Even more noticeable enhancements in S were observed in Sb/SbTe nanocomposites by Zhang et al. [16]. Fan et al. showed that the formation of nano-inclusions through melt spinning could lead to favorable conditions for thermoelectric applications [17]. Recently, Jiang et al. reported noticeable maximum *zT* values of 1.56 at 400 K by inducing PbSe nanocomposites with suppressed lattice and bipolar thermal conductivities that effectively inhibit minor charge carriers [18].

In this study, we investigated in situ phase segregation behavior during melt spinning with various metal elements, including Ti, V, Nb, Mo, W, Ni, Pd, and Cu, in *p*-type $Bi_{0.5}Sb_{1.5}Te_3$ (BST) thermoelectric alloys, which could be utilized for further investigation of a possible carrier filtering effect. The possible band alignments with secondary phases are presented with their measured thermoelectric properties.

2. Experimental Section

To prepare a set of samples of $Bi_{0.5}Te_{1.5}Se_3(M)_{0.1}$ (*M* = Ti, V, Nb, Mo, W, Ni, Pd, and Cu), all high-purity elements (Bi (99.999%, 5 N plus), Te (99.999%, 5 N plus), Se (99.999%, 5 N plus), and metal elements) were stoichiometrically synthesized by subsequent conventional melting and quenching techniques. The synthesized samples were blended using a ball-milling process (8000D, SPEX SamplePrep, Metuchen, NJ, USA) for 5 min. We conducted rapid solidification through melt spinning (Cu wheel rotation, 3600 rpm). The molten ingot was sprayed under a pressure of 0.03 MPa in an argon atmosphere. Using an agate mortar, the ribbons from the melt-spinning process were pulverized. Finally, the powders were sintered at 430 °C by spark plasma sintering (SPS) for 5 min under a pressure of 50 MPa.

To analyze the crystalline phases of the samples, X-ray diffraction (XRD, D8 Discover, Bruker, Billerica, MA, USA) was performed at room temperature. Then, the temperature-dependent σ and S parameters were measured simultaneously over the temperature range between room temperature and 480 K using a ZEM-3 measurement system (Advanced-RIKO, Yokohama, Japan) perpendicular to the SPS pressing direction. The κ values were also computed from the theoretical density (ρ_s), heat capacity (C_p), and thermal diffusivity (*D*) in the same direction ($\kappa = \rho_s \times C_p \times D$). Then, the diffusivities λ were measured by the laser flash method (LFA 467, Netzsch, Wittelsbacherstraße, Germany).

3. Results and Discussion

3.1. Secondary Phase Formation

Figure 1 shows the XRD patterns of the experimental samples of $Bi_{0.5}Sb_{1.5}Te_3(M)_{0.1}$ (*M* = Ti, V, Nb, Mo, W, Ni, Pd, and Cu). Each diffraction peak commonly showed its own matrix phase ($Bi_{0.5}Sb_{1.5}Te_3$, JCPDs PDF #49-1713) with the secondary phases, which was related to the added metals. The observed secondary phases were $TiTe_2$, VTe_2, $NbTe_2$, $MoTe_2$, W, $NiTe_2$, $PdTe_2$, and Cu_4Te_3 for various added metal elements (Ti, V, Nb, Mo, W, Ni, Pd, and Cu, respectively). Most secondary phases were formed as dichalcogenides, whereas the addition of Cu caused Cu_4Te_3 to form. The addition of W did not lead to the formation of compounds.
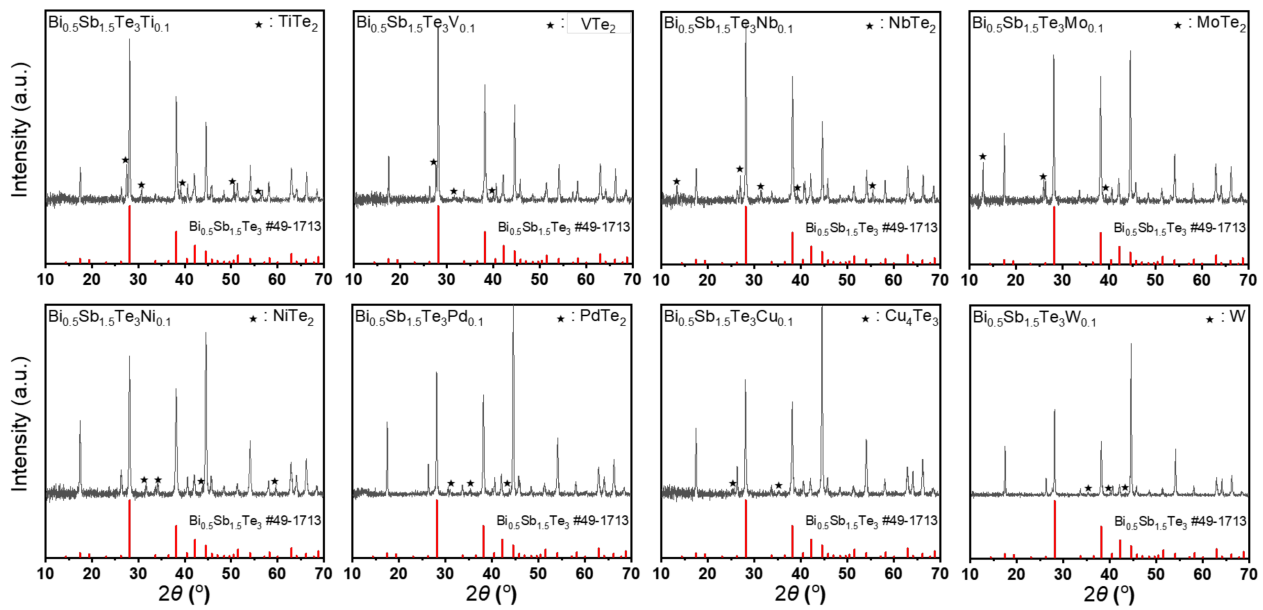
Figure 1. XRD patterns of $Bi_{0.5}Sb_{1.5}Te_3M_{0.1}$ (M = Ti, V, Nb, Mo, W, Ni, Pd and Cu).

3.2. Band Bending at Heterointerfaces

The band alignment schematics at the heterointerfaces between BST and the secondary phases are shown in Figures 2 and 3. Figure 2 shows the energy bands of the $Bi_{0.5}Sb_{1.5}Te_3(M)_{0.1}$ (M = Nb, Ni, W, Ti, and V) samples, whose secondary phases ($NbTe_2$, $NiTe_2$, W, $TiTe_2$, and VTe_2) were metallic. The work functions of $NbTe_2$, $NiTe_2$, W, $TiTe_2$, and VTe_2 were 4.62, 4.44, 4.5, 4.86, and 4.92 eV, respectively [19–21]. Possible carrier filtering barriers were formed in $Bi_{0.5}Sb_{1.5}Te_3Ni_{0.1}$, $Bi_{0.5}Sb_{1.5}Te_3Nb_{0.1}$, and $Bi_{0.5}Sb_{1.5}Te_3W_{0.1}$, with $NbTe_2$, $NiTe_2$, and $TiTe_2$ for hole transport, respectively. Their energy barrier heights were 0.08, 0.26, and 0.20 eV for $NbTe_2$, $NiTe_2$, and $TiTe_2$, respectively. For $Bi_{0.5}Sb_{1.5}Te_3V_{0.1}$ and $Bi_{0.5}Sb_{1.5}Te_3Ti_{0.1}$, no energy barrier was expected with the secondary phases of VTe_2 and $TiTe_2$, respectively.
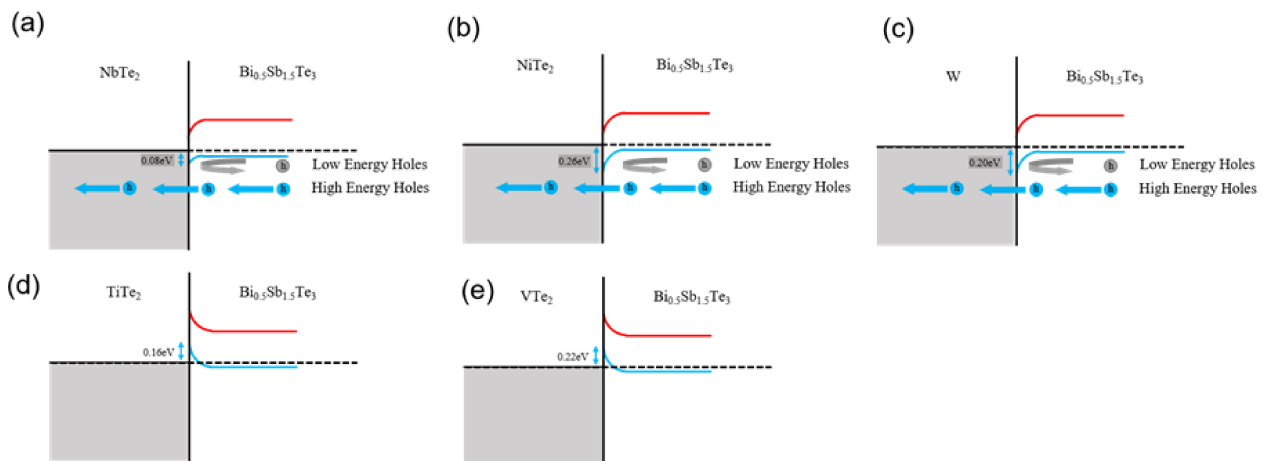
Figure 2. Band alignments at heterointerfaces between $Bi_{0.5}Sb_{1.5}Te_3$ and secondary phases ($NbTe_2$, $NiTe_2$, W, $TiTe_2$, and VTe_2).
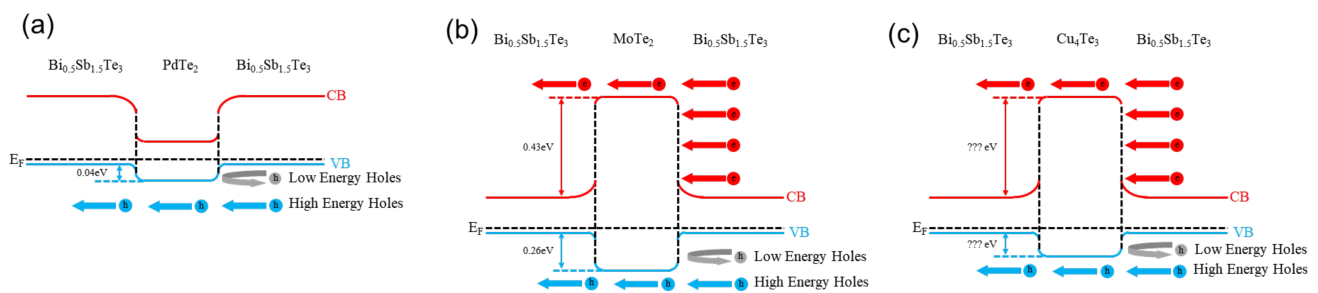
Figure 3. Band alignments in a $Bi_{0.5}Sb_{1.5}Te_3$–*M* heterojunction (*M* = semiconductor).

Figure 3 shows the energy bands of the $Bi_{0.5}Sb_{1.5}Te_3(M)_{0.1}$ (*M* = Pd, Mo, and Cu) samples, whose secondary phases ($PdTe_2$, $MoTe_2$, and Cu_4Te_3) were semiconducting. The band gap (E_g), Fermi level (E_f), and electron affinity (χ) of $PdTe_2$, $MoTe_2$, and Cu_4Te_3 were taken from the literature [19,22–24]. The χ of $Bi_{0.5}Sb_{1.5}Te_3$ is 4.50 eV and the E_g is 0.2 eV [25]. Given the band structure of $PdTe_2$, the band diagram of $Bi_{0.5}Sb_{1.5}Te_3Pd_{0.1}$ is presented in Figure 3a. A possible filtering barrier of 0.04 eV in $Bi_{0.5}Sb_{1.5}Te_3Pd_{0.1}$ is shown. In the case of $Bi_{0.5}Sb_{1.5}Te_3Mo_{0.1}$, because of the relatively wide E_g as compared to that of BST, an expected band diagram is given in Figure 3b. It formed a hole barrier of 0.26 eV, whereas the electron filtering barrier reached 0.43 eV. In the case of $Bi_{0.5}Sb_{1.5}Te_3Cu_{0.1}$, no band data were available for Cu_4Te_3. Because a quantitative illustration of the band diagram was unavailable, the illustration is shown with no quantitative values. Table 1 lists the work functions of E_g and χ for the segregated phases.

Table 1. Work functions or band gap (E_g) and electron affinity (χ) of the precipitates.

Properties	Phases	Work Function or E_g and χ (eV)	Reference
-	$Bi_{0.5}Sb_{1.5}Te_3$	E_g = 0.2 χ = 4.50	
Metallic	$TiTe_2$	4.86	[19]
	VTe_2	4.92	
	$NbTe_2$	4.62	
	W	4.5	[20]
	$NiTe_2$	4.44	[21,22]
Semi-conducting	$MoTe_2$	E_g = 0.8 χ = 4.29	[22]
	$PdTe_2$	E_g = 0.12 χ = 4.36	[23,24]
	Cu_4Te_3	unknown	-

3.3. Electronic Transport Properties (σ, S, and $S^2 \cdot \sigma$)

The temperature dependences of σ for $Bi_{0.5}Sb_{1.5}Te_3(M)_{0.1}$ (*M* = Ti, V, Nb, W, and Ni) are shown in Figure 4a. The σ value of the pristine BST sample was 767 S/cm at room temperature and decreased to 448 S/cm with increasing temperature. For the $Bi_{0.5}Sb_{1.5}Te_3Ti_{0.1}$ and $Bi_{0.5}Sb_{1.5}Te_3V_{0.1}$ samples, which did not form energy barriers at the heterointerfaces (Figure 2), the decreasing slope of σ with increasing temperature was much lower than that of the pristine BST, whereas the σ of $Bi_{0.5}Sb_{1.5}Te_3Ti_{0.1}$ and $Bi_{0.5}Sb_{1.5}Te_3V_{0.1}$ generally decreased and increased, respectively, as compared with that of the pristine BST. Note that these two samples did not form adequate energy barriers for hole carrier filtering (Figure 2); the work function of $TiTe_2$ and VTe_2 (4.86 and 4.92 eV, respectively) is much larger than the χ of the BST matrix (4.50 eV). The σ value of $Bi_{0.5}Sb_{1.5}Te_3Ti_{0.1}$ showed a lower σ value of 484 S/cm at room temperature. For the other samples (*M* = Nb, Ni, and W), the σ values all

increased, as compared with that of the pristine sample. The σ values of $Bi_{0.5}Sb_{1.5}Te_3Nb_{0.1}$ and $Bi_{0.5}Sb_{1.5}Te_3Ni_{0.1}$ reached their maxima at 2143 and 1154 S/cm at room temperature, respectively. The σ value of $Bi_{0.5}Sb_{1.5}Te3W_{0.1}$ was similar to that of the pristine BST at the measured temperatures.
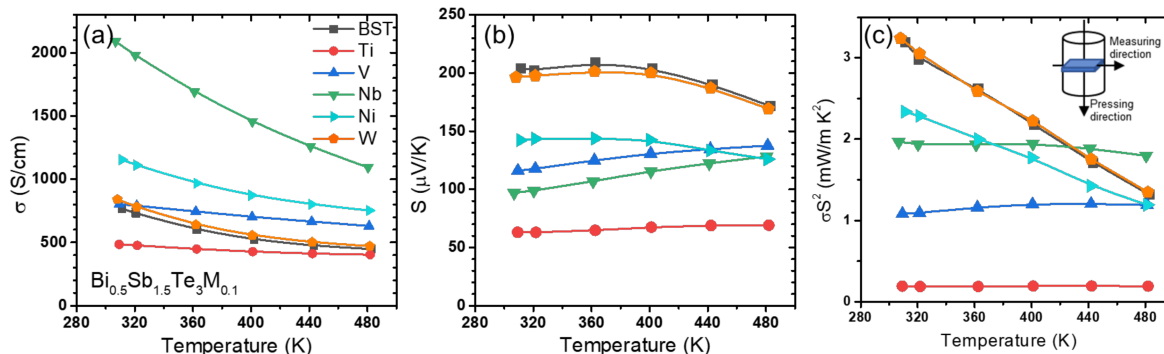
Figure 4. Temperature dependences of the (**a**) electrical conductivity, (**b**) Seebeck coefficient, and (**c**) power factor in $Bi_{0.5}Sb_{1.5}Te_3M_{0.1}$ (*M* = Ti, V, Nb, Mo and W).

S for the $Bi_{0.5}Sb_{1.5}Te_3(M)_{0.1}$ (*M* = Ti, V, Nb, W, and Ni) samples is given as a temperature-dependent function in Figure 4b. The *S* values of all the samples were suppressed as compared with that of the pristine BST. The BST sample had a peak *S* magnitude of 209 µV/K at 360 K and decreased to 171 µV/K with increasing temperature (at 480 K). At room temperature, *S* decreased to 194, 142, 117, 99, and 63 µV/K for the W-, Ni-, V-, Nb- and Ti- added samples, respectively.

Figure 4c shows the temperature dependence of $S^2 \cdot \sigma$ (power factor) for the $Bi_{0.5}Sb_{1.5}Te_3(M)_{0.1}$ (*M* = Ti, V, Nb, W, and Ni) samples. $Bi_{0.5}Sb_{1.5}Te_3W_{0.1}$ showed very similar power factor values to the pristine BST sample over the entire temperature range. The addition of W did not form the telluride, which generally only affects the electric transport of the BST matrix. Otherwise, the power factors decreased to 2.34, 1.97, 1.08, and 0.19 mW/mK^2 for the Ni-, Nb-, V-, and Ti-added samples. With the addition of Ti and V, which did not form energy barriers at the heterointerfaces with metallic $TiTe_2$ and VTe_2, σ and *S* decreased simultaneously, and the power factor was then reduced considerably. With the addition of Ni and Nb, which did form proper energy barriers at the heterointerfaces with metallic $NiTe_2$ and $NbTe_2$, σ increased significantly, whereas S decreased. As a result, the power factors were moderately reduced. For the Nb-added samples, the power factors at high temperatures of 440 and 480 K were higher than that of the pristine BST. For Ni- and Nb-added samples, further experiments with smaller additions of metal ($Bi_{0.5}Sb_{1.5}Te_3(M)_x$ (*M* = Ni and Nb, $x \leq 0.01$) were conducted to investigate the possible carrier filtering effect [26]. With a small addition of *x* = 0.01, power factor enhancements were observed with an increase in the effective mass, suggesting that a possible carrier filtering effect occurred.

The temperature dependences of σ for the $Bi_{0.5}Sb_{1.5}Te_3(M)_{0.1}$ (*M* = Mo, Pd, and Cu) samples, which exhibited semiconducting secondary phases, are shown in Figure 5a. Firstly, significant enhancements in the σ values were observed in the $Bi_{0.5}Sb_{1.5}Te_3(M)_{0.1}$ (*M* = Mo and Cu) samples.
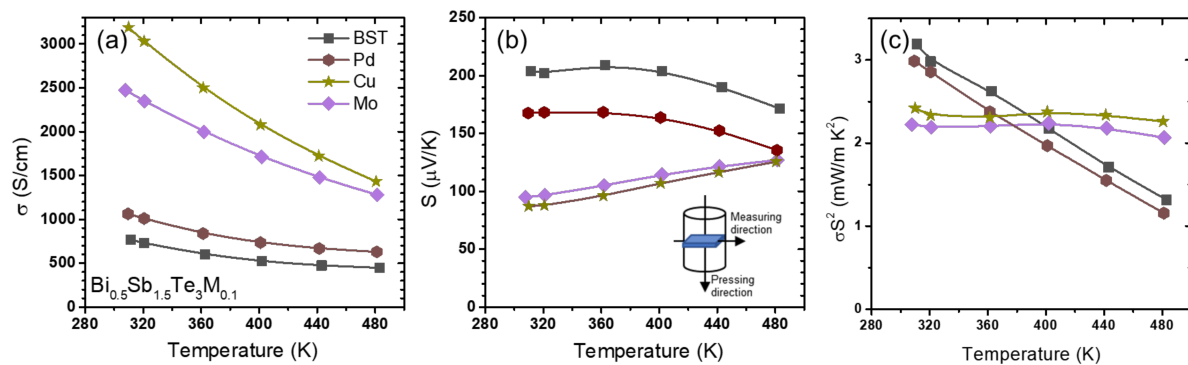
Figure 5. Temperature dependences of the (**a**) electrical conductivity, (**b**) Seebeck coefficient, and (**c**) power factor in $Bi_{0.5}Sb_{1.5}Te_3M_{0.1}$ (*M* = Ni, Pd and Cu).

The σ value of the $Bi_{0.5}Sb_{1.5}Te_3Cu_{0.1}$ sample showed a maximum of 3188 S/cm at 300 K, whereas that of the $Bi_{0.5}Sb_{1.5}Te_3Mo_{0.1}$ sample showed a maximum of 2494 S/cm. In the case of the $Bi_{0.5}Sb_{1.5}Te_3Pd_{0.1}$ sample, the maximum σ value was 1063 S/cm.

For $Bi_{0.5}Sb_{1.5}Te_3(M)_{0.1}$ (*M* = Mo, Pd, and Cu), S is given as a temperature-dependent function in Figure 5b. The *S* values for $Bi_{0.5}Sb_{1.5}Te_3 (M)_{0.1}$ (*M* = Mo, Pd, and Cu) were suppressed to 169, 98, and 85 μV/K as compared with 206 μV/K for the pristine BST sample at room temperature.

The temperature dependences of the power factors for the $Bi_{0.5}Sb_{1.5}Te_3(M)_{0.1}$ (*M* = Mo, Pd, and Cu) samples are shown in Figure 5c. The power factor of $Bi_{0.5}Sb_{1.5}Te_3Pd_{0.1}$ decreased slightly as compared with that of the pristine BST. For the Pd- and Cu-added samples, the power factors decreased further, to 2.42 and 2.23 mW/mK^2, respectively, at room temperature, and greater values were observed at higher temperatures above 400 K.

3.4. Thermal Conductivity (κ_{tot}, κ_{elec}, κ_{latt})

To further investigate the total thermal conductivity (κ_{tot}) behavior in $Bi_{0.5}Sb_{1.5}Te_3(M)_{0.1}$ (*M* = Ti, V, Nb, Mo, W, Ni, Pd, and Cu), we determined the κ_{tot} values to be mainly binary parts of thermal conductivity, namely, κ_{ele} and κ_{latt}. They were calculated using the following equation:

$$\kappa_{tot} = \kappa_{ele} + \kappa_{latt} \tag{1}$$

The κ_{ele} values were calculated using the Wiedemann–Franz equation, as follows:

$$\kappa_{ele} = L \times \sigma \times T \tag{2}$$

where *L* is the Lorenz number (calculated as $L = 1.5 + \exp(-|S|/116)$). *L* and *S* are treated as units in terms of 10^{-8} WΩK^{-2} and μV/K, respectively [27].

The κ_{tot} and κ_{latt} values for the $Bi_{0.5}Sb_{1.5}Te_3(M)_{0.1}$ (*M* = Ti, V, Nb, Ni, and W) samples, as functions of temperature, are shown in Figure 6a,b, respectively. As shown in Equation (1), we computed the κ_{latt} values by subtracting the κ_{ele} values (which were calculated in advance) from the κ_{tot} values. The κ_{latt} values of the standard BST sample were increased from 0.99 to 1.42 W/mK as the measuring temperature increased. For the $Bi_{0.5}Sb_{1.5}Te_3Ni_{0.1}$ sample, κ_{tot} and κ_{latt} increased. κ_{latt} was significantly reduced for the V- and Nb-added samples. The addition of W did not form the telluride, which seemed to not affect the thermal conductivity of the BST matrix much.
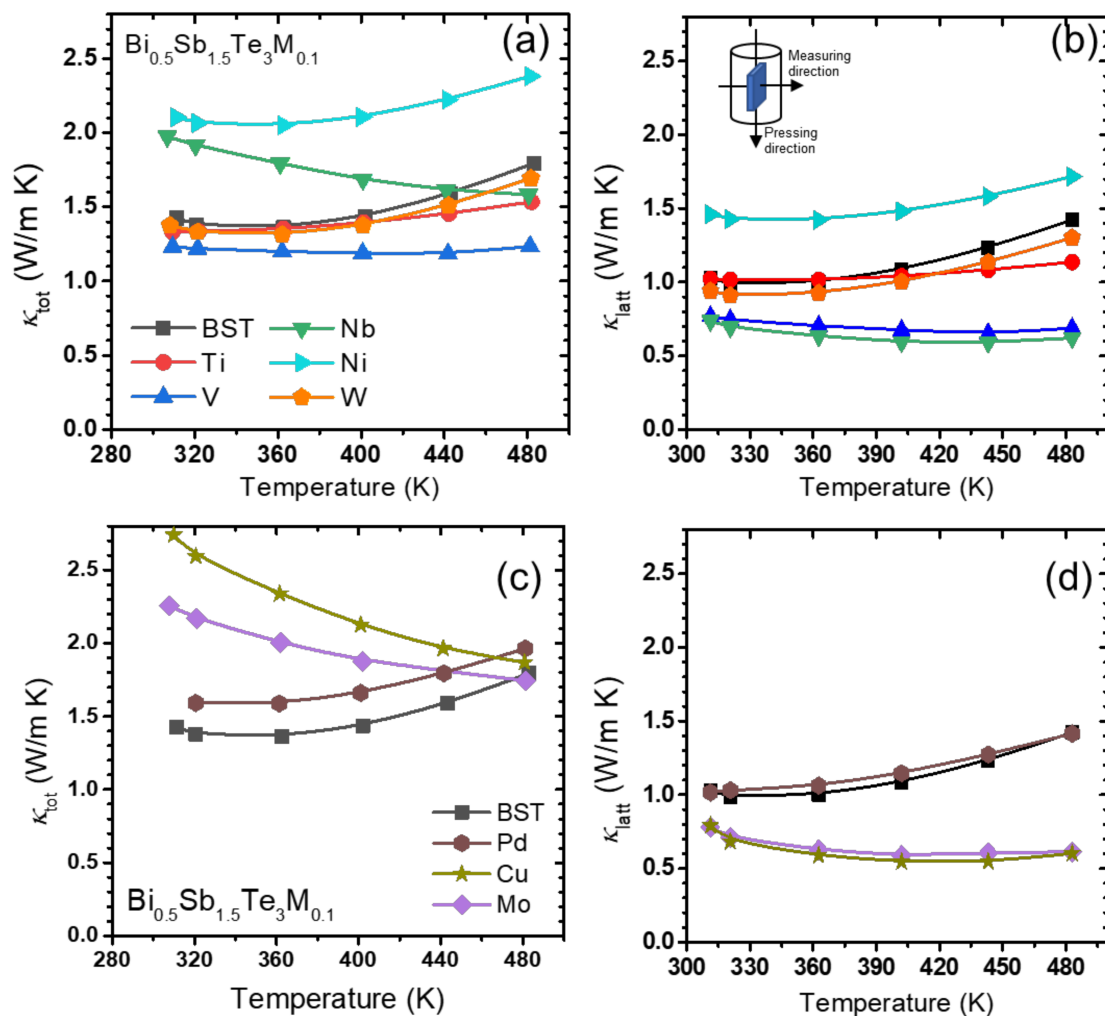
Figure 6. (**a**) κ_{tot} and (**b**) κ_{latt} as a function of temperature for $Bi_{0.5}Sb_{1.5}Te_3M_{0.1}$ (M = Ti, V, Nb, Ni and W); (**c**) κ_{tot} and (**d**) κ_{latt} as a function of temperature for $Bi_{0.5}Sb_{1.5}Te_3M_{0.1}$ (M = Ni, Pd and Cu).

The κ_{tot} and κ_{latt} values, as functions of temperature, for the $Bi_{0.5}Sb_{1.5}Te_3(M)_{0.1}$ (M = Mo, Pd, and Cu) samples are shown in Figure 6c,d. For the $Bi_{0.5}Sb_{1.5}Te_3Pd_{0.1}$ samples, the general behavior of κ_{tot} and κ_{latt} with temperature were relatively similar to that of the pristine BST. $Bi_{0.5}Sb_{1.5}Te_3(M)_{0.1}$ (M = Cu and Mo) with higher σ values (Figure 5a) exhibited a much higher κ_{tot} and showed a gradual decrease with increasing temperature. The κ_{latt} for $Bi_{0.5}Sb_{1.5}Te_3(M)_{0.1}$ (M = Cu and Mo) was much lower than that of the pristine BST. In all the samples that formed tellurides, except for the Nb- and Pd-added samples, some degrees of reduction in κ_{latt} were shown due to the presence of secondary phases, as observed in Figure 6 [28]. However, adding Nb or Pd, which form $NbTe_2$ and $PdTe_2$, respectively, increased the κ_{latt}, or had little effect. At this stage, these different results cannot be elaborated. Further investigation into the possible carrier filtering effects of smaller amounts of Nb- and Pd-added Bi_2Te_3-based alloys showed a small degree of reduction in κ_{latt} [26,29].

3.5. Thermoelectric Figure of Merit zT

All the measured values of S, σ, and κ_{tot} for all the specimens were used to determine the figure of merit zT. The figure of merit zT values are shown in Figure 7a,b. In Figure 7a, the Ti-added samples, which showed a significantly reduced power factor due to the simultaneous reduction of σ and S, exhibited a considerably reduced zT. For the Ni-added sample, a lower zT was observed under all temperatures, which was mainly due to the increased κ_{tot} and κ_{latt}. Therefore, the $Bi_{0.5}Sb_{1.5}Te_3(M)_{0.1}$ (M = Ti and Ni) samples showed

a lower zT over the entire temperature range. For the $Bi_{0.5}Sb_{1.5}Te_3(M)_{0.1}$ (M = V and Nb) samples, the zT at low temperatures decreased, whereas that at a high temperature (480 K) exhibited a slightly higher value as compared with the zT values of the pristine BST. The addition of W did not form any chalcogenides, which seemed to affect the thermal conductivity of the BST matrix. It showed an improvement in zT of approximately 5% as compared with that of the pristine BST. In Figure 7b, the Pd-added samples, which showed a moderately decreased power factor with slightly increased κ_{tot} and κ_{latt}, exhibited a reduced zT over the entire temperature range. In the range of 300–440 K, the $Bi_{0.5}Sb_{1.5}Te_3(M)_{0.1}$ (M = Mo, and Cu) samples had lower zT values than that of the pristine BST. However, from 440 K to 480 K, the $Bi_{0.5}Sb_{1.5}Te_3(M)_{0.1}$ (M = Mo, and Cu) samples had slightly higher zT values than that of the pristine BST.
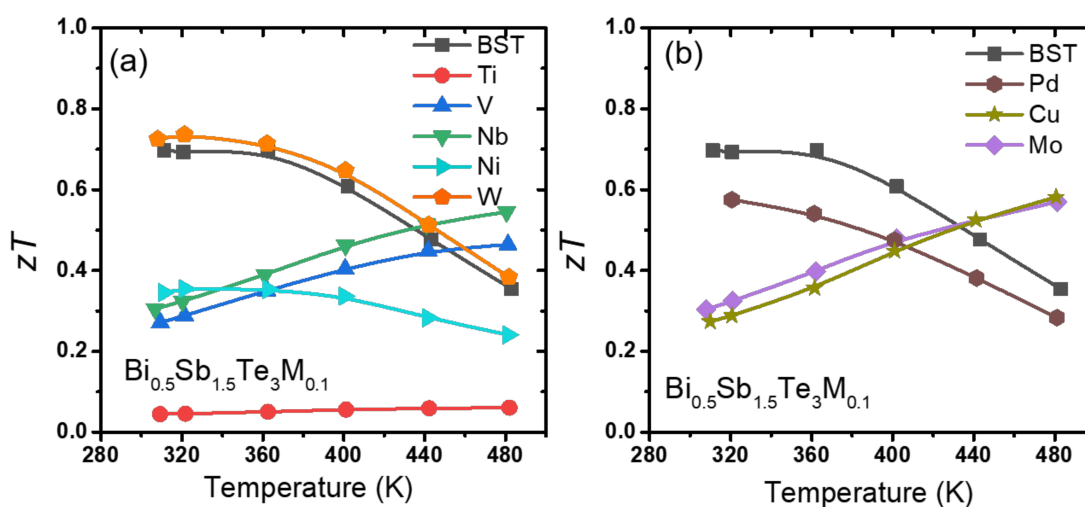
Figure 7. Figure of merit zT of (**a**) $Bi_{0.5}Sb_{1.5}Te_3M_{0.1}$ (M = Ti, V, Nb, Mo and W) and (**b**) $Bi_{0.5}Sb_{1.5}Te_3M_{0.1}$ (M = Ni, Pd and Cu).

4. Conclusions

We investigated the in situ phase segregation behavior during melt spinning with various metal elements, including Ti, V, Nb, Mo, W, Ni, Pd, and Cu, in *p*-type $Bi_{0.5}Sb_{1.5}Te_3$ (BST) thermoelectric alloys. The observed secondary phases were $TiTe_2$, VTe_2, $NbTe_2$, $MoTe_2$, W, $NiTe_2$, $PdTe_2$, and Cu_4Te_3 for various added metal elements (Ti, V, Nb, Mo, W, Ni, Pd, and Cu, respectively). The electrical conductivity, Seebeck coefficient, and thermal conductivity of the BST composite with various secondary phases were measured and compared with those of the pristine BST alloys. The possible band alignments with the secondary phases were introduced, which could be utilized for further investigation of a possible carrier filtering effect when forming nanocomposites.

Author Contributions: Conceptualization, D.H.K. and T.K.; methodology, S.W.L.; formal analysis, D.H.K.; investigation, D.H.K.; data curation, H.-S.K.; writing—original draft preparation, D.H.K. and T.K.; writing—review and editing, W.H.S.; supervision, S.-i.K.; project administration, S.-i.K. All authors have read and agreed to the published version of the manuscript.

Institutional Review Board Statement: Not applicable.

Informed Consent Statement: Not applicable.

Data Availability Statement: Data available on request.

Conflicts of Interest: The authors declare no competing financial interest.

References

1. Snyder, G.J.; Toberer, E.S. Complex thermoelectric materials. *Nat. Mater.* **2008**, *7*, 105–114. [CrossRef] [PubMed]
2. Bell, L.E. Cooling, Heating, Generating Power, and Recovering Waste Heat with Thermoelectric Systems. *Science* **2008**, *321*, 1457–1461. [CrossRef]
3. Zhang, Q.; Cao, F.; Liu, W.; Lukas, K.; Yu, B.; Chen, S.; Opeil, C.; Broido, D.; Chen, G.; Ren, Z.F. Heavy Doping and Band Engineering by Potassium to Improve the Thermoelectric Figure of Merit in p-Type PbTe, PbSe, and PbTe$_{1-y}$Se$_y$. *J. Am. Chem. Soc.* **2012**, *134*, 10031–10038. [CrossRef] [PubMed]
4. Liu, W.; Hu, J.; Zhang, S.; Deng, M.; Han, C.G.; Liu, Y. New trends, strategies and opportunities in thermoelectric materials: A perspective. *Mater. Today Phys.* **2017**, *1*, 50–60. [CrossRef]
5. Tan, G.; Shi, F.; Hao, S.; Zhao, L.D.; Chi, H.; Zhang, X.; Uher, C.; Wolverton, C.; Dravid, V.P.; Kanatzidis, M.G. Non-equilibrium processing leads to record high thermoelectric figure of merit in PbTe-SrTe. *Nat. Commun.* **2016**, *7*, 12167. [CrossRef]
6. Kim, H.S.; Lee, K.H.; Yoo, J.Y.; Shin, W.H.; Roh, J.W.; Hwang, J.Y.; Kim, S.W.; Kim, S.I. Suppression of bipolar conduction via bandgap engineering for enhanced thermoelectric performance of p-type Bi$_{0.4}$Sb$_{1.6}$Te$_3$ alloys. *J. Alloy. Compd.* **2018**, *741*, 869–874. [CrossRef]
7. Lee, K.-H.; Hwang, S.; Ryu, B.; Ahn, K.; Roh, J.; Yang, D.; Lee, S.-M.; Kim, H.; Kim, S.-I. Enhancement of the Thermoelectric Performance of Bi$_{0.4}$Sb$_{1.6}$Te$_3$ Alloys by In and Ga Doping. *J. Electron. Mater.* **2012**, *42*, 1617–1621. [CrossRef]
8. Choi, J.; Lee, J.Y.; Lee, S.-S.; Park, C.R.; Kim, H. High-Performance Thermoelectric Paper Based on Double Carrier-Filtering Processes at Nanowire Heterojunctions. *Adv. Energy Mater.* **2016**, *6*, 1502181. [CrossRef]
9. Lee, K.-H.; Kim, H.-S.; Kim, S.-I.; Lee, E.-S.; Lee, S.-M.; Rhyee, J.-S.; Jung, J.-Y.; Kim, I.-H.; Wang, Y.; Koumoto, K. Enhancement of Thermoelectric Figure of Merit for Bi$_{0.5}$Sb$_{1.5}$Te$_3$ by Metal Nanoparticle Decoration. *J. Electron. Mater.* **2012**, *41*, 1165–1169. [CrossRef]
10. Lan, Y.; Minnich, A.J.; Chen, G.; Ren, Z. Enhancement of thermoelectric figure-of-merit by a bulk nanostructuring approach. *Adv. Funct. Mater.* **2010**, *20*, 357–376. [CrossRef]
11. Liu, Y.; Wang, W.; Yang, J.; Li, S. Recent Advances of Layered Thermoelectric Materials. *Adv. Sustain. Syst.* **2018**, *2*, 180046.
12. Eivari, H.A.; Sohbatzadeh, Z.; Mele, P.; Assadi, M.H.N. Low thermal conductivity: Fundamentals and theoretical aspects in thermoelectric applications. *Mater. Energy Today* **2021**, *21*, 100744. [CrossRef]
13. Loffe, A.F.; Stil'bans, L.S.; Iordanishvili, E.K.; Stavitskaya, T.S.; Gelbtuch, A.; Vineyard, G. Semiconductor Thermoelements and Thermoelectric Cooling. *Phys. Today* **1957**.
14. Gayner, C.; Amouyal, T. Energy Filtering of Charge Carriers: Current Trends, Challenges, and Prospects for Thermoelectric Materials (Progress Report). *Adv. Func. Mat.* **2020**, *30*, 1901789. [CrossRef]
15. Dou, Y.C.; Qin, X.Y.; Li, D.; Li, L.L.; Zou, T.H.; Wang, Q.Q. Enhanced thermopower and thermoelectric performance through energy filtering of carriers in (Bi$_2$Te$_3$)$_{0.2}$(Sb$_2$Te$_3$)$_{0.8}$ bulk alloy embedded with amorphous SiO$_2$ nanoparticles. *Int. J. Appl. Phys.* **2013**, *114*, 044906. [CrossRef]
16. Zhang, Z.; Wu, Y.; Zhang, H.; Zeng, Z.; Hu, Z. Enhancement of Seebeck coefficient in Sb-rich Sb$_2$Te$_3$ thin film. *J. Mater. Sci. Mater. Electron.* **2015**, *26*, 1619–1624. [CrossRef]
17. Fan, S.; Zhao, J.; Guo, J.; Yan, Q.; Ma, J.; Hng, H.H. p-type Bi$_{0.4}$Sb$_{1.6}$Te$_3$ nanocomposites with enhanced figure of merit. *Appl. Phys. Lett.* **2010**, *96*, 182104. [CrossRef]
18. Jiang, Z.; Ming, H.; Qin, X.; Feng, D.; Zhang, J.; Song, C.; Li, D.; Xin, H.; Li, J.; He, J. Achieving High Thermoelectric Performance in p-Type BST/PbSe Nanocomposites through the Scattering Engineering Strategy. *ACS Appl. Mater. Interfaces* **2020**, *12*, 46181–46189. [CrossRef] [PubMed]
19. Zhang, C.; Gong, C.; Nie, Y.; Min, K.-A.; Liang, C.; Oh, Y.J.; Zhang, H.; Wang, W.; Hong, S.; Colombo, L.; et al. Systematic study of electronic structure and band alignment of monolayer transition metal dichalcogenides in Van der Waals heterostructures. *2D Mater.* **2016**, *4*, 015026. [CrossRef]
20. Davisson, C.; Germer, L.H. The Thermionic Work Function of Tungsten. *Phys. Rev.* **1922**, *20*, 300–330. [CrossRef]
21. Lebègue, S.; Björkman, T.; Klintenberg, M.; Nieminen, R.M.; Eriksson, O. Two-Dimensional Materials from Data Filtering and Ab Initio Calculations. *Phys. Rev. X* **2013**, *3*, 031002.
22. Aftab, S.; Iqbal, M.W.; Afzal, A.M.; Khan, M.F.; Hussain, G.; Waheed, H.S.; Kamran, M.A. Formation of an MoTe2 based Schottky junction employing ultra-low and high resistive metal contacts. *RSC Adv.* **2019**, *9*, 10017–10023. [CrossRef]
23. Qu, Y.; Kwok, C.T.; Shao, Y.; Shi, X.; Kawazoe, Y.; Pan, H. Pentagonal transition-metal (group X) chalcogenide monolayers: Intrinsic semiconductors for photocatalysis. *Int. J. Hydrog. Energy* **2021**, *46*, 9371–9379. [CrossRef]
24. Jiajun, L. First-Principles Study on Si24 and 2D Material Heterostructures for Solar Cell Applications. Ph.D. Thesis, National University of Singapore, Singapore, 2017.
25. Kim, S.I.; Kim, S.W.; Roh, J.W.; Ahn, K.; Yeon, D.H.; Lee, K.H. Experimental evidence of enhancement of thermoelectric properties in tellurium nanoparticle-embedded bismuth antimony telluride. *J. Mater. Res.* **2012**, *27*, 2449–2456. [CrossRef]
26. Kim, H.-S.; Kim, T.; An, J.; Kim, D.; Jeon, J.H.; Kim, S.-I. Segregation of NiTe$_2$ and NbTe$_2$ in p-Type Thermoelectric Bi$_{0.5}$Sb$_{1.5}$Te$_3$ Alloys for Carrier Energy Filtering Effect by.Melt Spinning. *Appl. Sci.* **2021**, *11*, 910. [CrossRef]
27. Kim, H.-S.; Gibbs, Z.M.; Tang, Y.; Wang, H.; Snyder, G.J. Characterization of Lorenz number with Seebeck coefficient measurement. *APL Mater.* **2015**, *3*, 041506. [CrossRef]

28.　Lee, K.H.; Kim, Y.-M.; Park, C.O.; Shin, W.H.; Kim, S.W.; Kim, H.-S.; Kim, S.-I. Cumulative defect structures for experimentally attainable low thermal conductivity in thermoelectric (Bi,Sb)$_2$Te$_3$ alloys. *Mater. Energy Today* **2021**, *21*, 100795. [CrossRef]

29.　Kim, D.H.; Kim, H.-S.; Hong, S.; Lee, J.H.; Han, J.G.; Cho, H.S.; Lee, S.W.; Kim, S.-I. Investigation of PdTe2 Phase Segregation on Thermoelectric Properties of n-Type Bi$_2$Te$_{2.7}$Se$_{0.3}$ Fabricated by Melt-Spinning Technique for Possible Carrier Filtering Effect. *Electron. Mater. Lett.* **2021**, *17*, 436–442. [CrossRef]